

# Computational Biological Fluid Dynamics: Digitizing and Visualizing Animal Swimming and Flying<sup>1</sup>

HAO LIU<sup>2</sup>

*Computer and Information Division, The Institute of Physical and Chemical Research (RIKEN),  
2-1 Hirosawa, Wako-shi, Saitama 351-0198, Japan*

**SYNOPSIS.** Characterized by complex geometry and complicated dynamic process, biological fluid dynamics in swimming and flying is usually of large scale vortex flows with four-dimensional nature, namely, spatial three-dimensional and one-dimensional in time. Conventional theories for understanding power and energetics in swimming and flying rely exclusively on the consistent potential flow formulation in qualitatively analyzing the physics as well as the observations and measurements in visualizing the flows so as to support the theories. In the present paper we address a new paradigm of the so-called, *simulation-based biological fluid dynamics* that can digitize and visualize swimming and flying by using computational mechanical modeling of the biological fluid dynamics through faithful reconstruction of morphology and realistic representation of kinematics of an individual object. We demonstrate an integrated computational system as a baseline for the simulation-based biological fluid dynamics, which involves four subsystems of the morphological modeling, the kinematic modeling, the computational fluid dynamic modeling, and the post-processing for visualization. Applications of a realistic model of insect flapping flight and an extensive study on the Micro Air Vehicle are then presented and discussed.

## INTRODUCTION

Fluid dynamic phenomena in animal locomotion are complicated because biological fluid dynamics involves the interaction of elastic or even flexible living tissues with surrounding viscous fluid. The biological fluid dynamic phenomena are, in general, characterized by large-scale vortex structure because of the highly unsteady motions, the complex, variable geometry of the object in swimming and flying. The feature of the biological fluid dynamics may be illustrated as shown in Figure 1, by means of a schematic diagram of relationship between organ sizes such as body length or wing length and the Reynolds number that is a ratio of inertia-to-viscous force. It is seen that most swimming and flying with a representative length on the order of centimeter are observed over a range of intermediate Reynolds numbers from order of  $10^0$  for a tiny insect of thrips up to order of  $10^4$  for moth, where inertial force and viscous force are equivalent, generally resulting in complicated vortex flow (Triantafyllou, 1995; Ellington, 1995). Hence, prediction of power and energetics in swimming and flying needs to correctly understand and accurately quantify such large-scale vortex flows.

Most aquatic animals use the jet-stream propulsion in a form of propagating a transverse wave along the body from head to tail. This swimming as shown in Figure 1, covering a wide range of Reynolds numbers from order of  $10^2$  for tadpole larvae up to order of  $10^8$  for the most rapid cetacean, has been observed to be the most effective movement of swimming propulsion. Conventionally, approaches established on a basis of

potential flow formulation, linearized body boundary conditions, and an assumed shape for the wake were proposed by many pioneering researchers (Lighthill, 1969, 1975; Wu, 1971; Newman, 1973), that were further extended to a three-dimensional waving plate theory later (Cheng *et al.*, 1991); but they could neither solve the nonlinear flow-body interaction nor allow the wake dynamics to develop. Experimentally, some studies (Triantafyllou, 1993, 1995) of propulsion of oscillating hydrofoils to correlate the relationship between mechanical propulsive efficiency and a dimensionless frequency, namely, Strouhal number have given an evidence that an optimal efficiency is achieved when a staggered array of reverse von Karman vortices is formed in the wake within a narrow range of the Strouhal number, and this occurs for most fishes with a range from 0.25 to 0.35. Compared with fish propulsion, studies on mechanisms of fish maneuvering as fast-start swimming are quite limited because of its highly unsteady fluid dynamics. Recently, some experimental approaches have been reported by means of advanced measuring techniques like digital particle image velocimetry (Domenici and Blake, 1997; Johnson *et al.*, 1998; Druke and Lauder, 1999, 2001), and this strongly depends upon the development of high-tech-based measuring methods. Actually, what law of hydrodynamic such high-efficiency or large-thrust swimming mechanism obeys and how the relationship between three-dimensional geometry and swimming mode of a realistic vertebrate locomotor affect their propulsion are not very well understood.

Flying animals, in general, perform flapping wing flight because they have to create not only lift to stay on the airborne but also thrust for forward and darting flight, in achieving remarkable maneuvers with rapid accelerations and decelerations. In the past decade, a growing group of mathematicians, biologists, zoolo-

<sup>1</sup> From the Symposium *Dynamics and Energetics of Animal Swimming and Flying* presented at the Annual Meeting of the Society for Integrative and Comparative Biology, 2–6 January 2002, at Anaheim, California.

<sup>2</sup> E-mail: hliu@postman.riken.go.jp

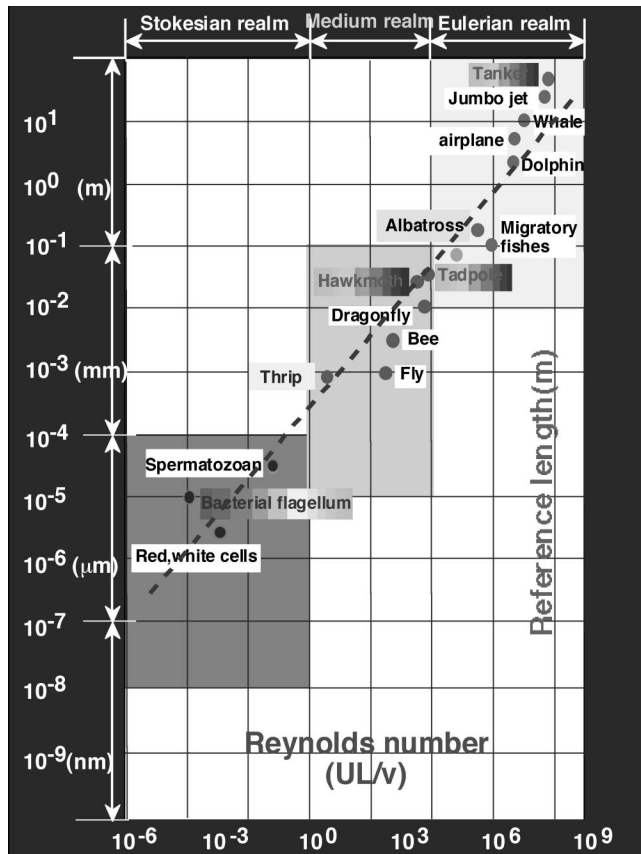


FIG. 1. A schematic diagram of relationship between organ size and Reynolds number. Most swimming and flying with a representative length on the order of centimeter are observed over a range of intermediate Reynolds numbers from order of  $10^0$  up to order of  $10^4$ , where inertial and viscous forces are equivalent, generally resulting in large-scale vortex structure.

gists and aeronautical engineers have been endeavoring to construct appropriate aerodynamic models (Lighthill, 1975; Rayner, 1979; Maxworthy, 1979; Pennycuik, 1989; Norberg, 1990; Spedding, 1992; Ellington, 1995; Azuma, 1983; Weis-Fogh, 1972). Conventionally, methods based on the “quasi-steady assumption” have been used to explain the aerodynamics of insect flight, that consider the instantaneous force on a flapping wing to be the same as that, which would be experienced, in steady motion at the same instantaneous velocity and angle of attack (Lighthill, 1975). These models suggested that, by ignoring any influence of the past history of the wing motion (which greatly simplifies the dynamic problem to a sequence of independent, static conditions), the ‘steady’ aerodynamic mechanisms might be sufficient to explain flight in most insect species (Ellington, 1995). However, recent studies, involving detailed quasi-steady analyses of the aerodynamic forces (Ellington, 1995) or direct measurements of the instantaneous forces generated by tethered insects (Cloupeau, 1979; Wilkin and Williams, 1993) have shown that the lift force which it predicts is insufficient to support the insect body weight. More recently, two breakthrough studies

(Ellington, 1998 and Dickinson, 1999) by means of robotic flappers that mimic basic movements of flapping wings of insects and some new flow visualization methods like particle image velocimetry techniques, have unveiled some brand-new understandings of insect flapping flight mechanism. However, as a result of the large-scale unsteady motions, the complex, variable geometry of the wing, and the complicated vortex flow structure, the aerodynamics on the flapping wing, in particular on the forward flight and maneuvering, in fact, still remain not very clear yet.

In this review paper, we address a new paradigm of the *simulation-based biological fluid dynamics*, which, by directly solving the full Navier-Stokes equations through computer simulation, can digitize and visualize swimming and flying to provide detailed information of physical variables such as velocity and pressure at macro- and microscopic level, and hence give an overall understanding of the physical phenomena. A baseline for this paradigm is an integrated computational system, involving a morphological modeling subsystem, a kinematic modeling subsystem, a computational fluid dynamics (CFD) modeling subsystem, and a post-processing subsystem for visualization. The integrated system developed has been validated to be feasible in modeling complicated biological fluid dynamics, through a series of stepwise baseline benchmark tests and applications for realistic modeling of hydro- and aerodynamics of undulatory swimming and insect flight (Liu, 1995; Liu *et al.*, 1996, 1997, 1998; Liu and Kawachi, 1998, 1999, 2001). In the following, we first give a detailed description of the computational mechanical system with specific focus on the morphological modeling and on the kinematic modeling. Then we present results about a realistic moth’s model and address an overall understanding of the complicated vortex structures around a 3D flapping wing during the complete cycle of translational and rotational motions, as well as the corresponding time course of instantaneous force-production. We further demonstrate results of a rotary wing model and discuss the discrepancy of the leading-edge vortex feature as well as the aerodynamic characteristics compared with the flapping wing.

## MATERIALS AND METHODS

### Morphological modeling

Morphological modeling or geometric modeling plays a key role in determining local three-dimensional flow feature. In animal locomotion, the morphological modeling often points to digitizing an object, *i.e.*, the reconstruction of a 3D geometry on a basis of two-dimensional images of the object. The geometric model should not only be for visualizing the object in terms of surface/volume rendering but also be specified for computational mechanical modeling of fluid dynamics in swimming and flying in terms of domain discretization, *i.e.*, the gridding. The morphological modeling can be clarified in four-folded: 1) *imaging*, which pro-

vides 2D pixel data for 2D slice images or 3D voxel data for 3D images; 2) *segmentation* of the required object, which points to extracting the configuration of the object in terms of wire frame and/or skeleton model by means of appropriate image-processing techniques; 3) *smoothing and curve / surface fitting*, which are often implemented for the reconstructed model as well as its geometric characteristics like curvature; 4) *modeling and domain discretization*, which involve surface and/or volume rendering of the reconstructed object as well as the computational domain decomposition in terms of grids. We have developed a feasible and efficient computer-aided method that is capable to unify the geometric modeling and the kinematic modeling associated with three-dimensional, swimming and flying locomotors. This method is established with consideration of a fact that the geometry of most locomotive animals can be well defined by using a skeleton or axis running through the object in combination with configurations or sliced cross sections perpendicular to the axis. With definition of the time-variation of the body skeleton, this method substantially can unify the modeling of both geometry and kinematics in swimming and flying. Another advantage of the methodology is that computational grids around the object undergoing swimming or flying can be generated simultaneously and also be easily regenerated to match the moved or deformed boundary surfaces of the locomotors.

The pre-processing, *i.e.*, the *imaging* is to provide proper and sufficient images to define a spatial curve of the axis as well as the relative position and the configuration of each cross section along the axis in a manner of a set of spatial discretized points. The digitized geometry (Fig. 2) of a tadpole model (Liu and Kawachi, 1999) was reconstructed based on a side-and-top view picture of the bullfrog, *Rana catesbeiana*. The skeleton of the tadpole was defined as the centerline axis of the body. Geometry of the moth's wing (Fig. 3) was modeled based on a tracing of the outline of a fore-and hind wing of a *Manduca sexta*, with the spanwise axis running one-quarter of chord length from the leading-edge. A uniform thickness was taken but with an elliptic smoothing at the leading- and trailing edge as well as at the tip. Since the main spars of insect wings radiate from the bases of the wings, we built the wing configuration (the spanwise grid lines on the wing surface) in a similar manner (Liu and Kawachi, 1998).

#### Kinematic modeling

Kinematic modeling of the movements of bodies, fins, and wings in swimming and flying, if using the method as described in the preceding section, can be transferred to define the time-varying motions of the reconstructed skeleton of the object. Given  $N$  (1, 2, 3,  $n$ , ...,  $N$ ) sets of images of the object in a complete stroke or beat cycle, this can be achieved either by repeating the procedure in the morphological modeling at  $n$  instance, or by directly defining the 3D motions

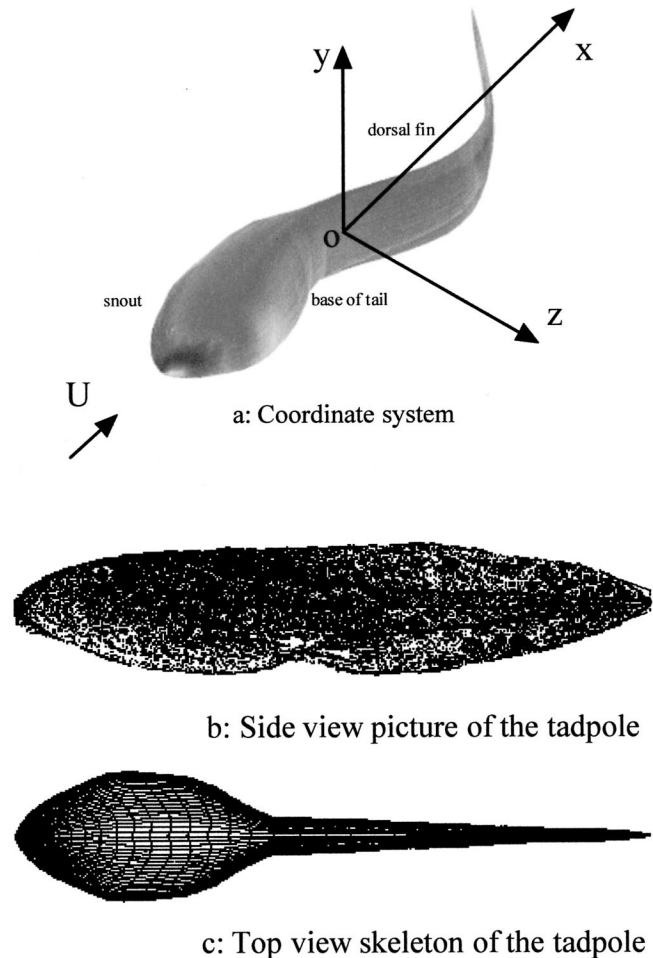


FIG. 2. A computer model of tadpole: a) definition of the body-fixed system; b) a tadpole image in side view; and c) a top view of the skeleton tadpole model.

of the skeleton of the object with assumption of unchangeable cross sections with time. The latter method is simple because only one geometric model is built up and the movements of the object are merely defined for the skeleton. This method was utilized in both swimming and flying modeling.

The kinematic models for undulatory swimming can be approximated very well based on the movements of its centerline axis of the object. A 3D tadpole kinematic model by the author (Liu *et al.*, 1997) was successfully established, based on the straight forward locomotion of a *Rana catesbeiana* larva, swimming under two basic assumptions of 1D lateral traveling wave like a waving plate propagating down the body towards the tail tip, and elongation of body length during undulatory swimming. A sinusoidal swimming mode based on the longitudinal coordinates (Fig. 2) has a waveform as:

$$z_i = h_i(x, t) = a_i(x) \sin \left[ 2\pi \left( \frac{x}{\lambda} - \frac{t}{T} \right) \right], \quad (1)$$

where  $a_i(x)$  represents amplitude,  $\lambda$  is wavelength,  $T$  is



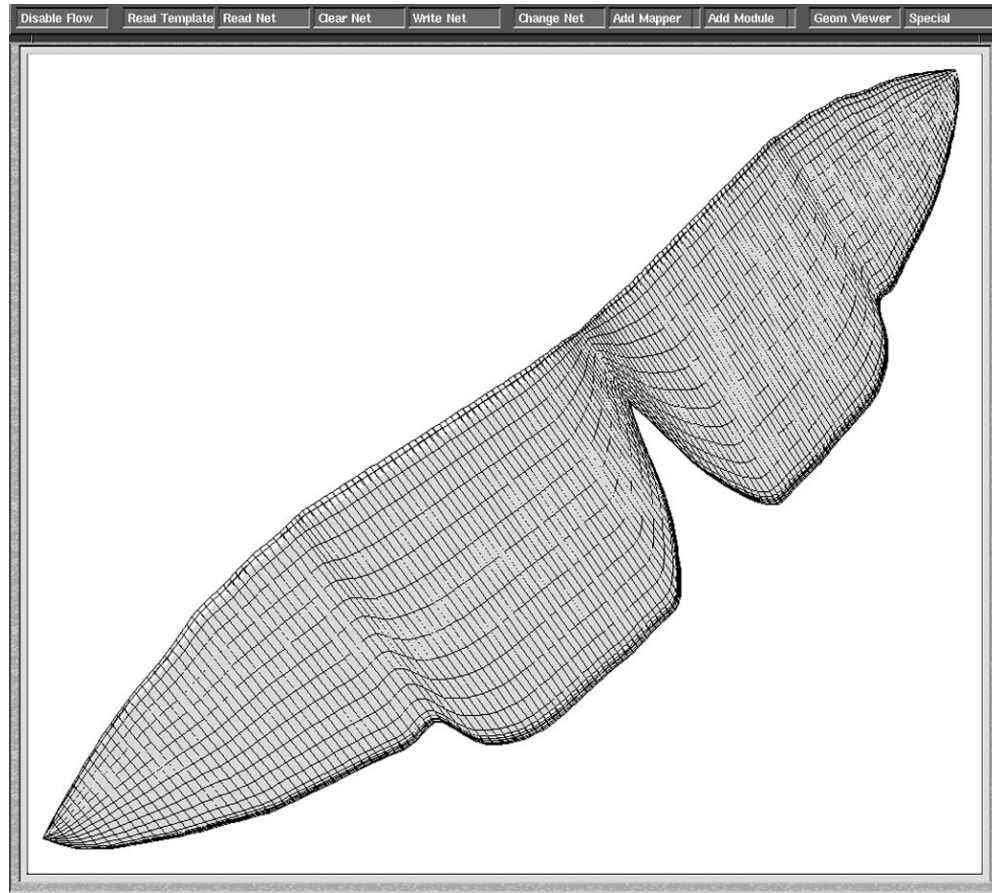


FIG. 3. A computational geometric model of hawkmoth's wing.

period,  $h_i(x, t)$  denotes the center plane of the tadpole model,  $t$  is time and  $x$  is the coordinate in  $x$ -direction corresponding to the body length. The amplitudes of  $a_i(x)$ , are determined by using the spline interpolation from five original maximum amplitudes,  $a_i$ , along the length,  $L$ , of the tadpole. These values are: at the snout ( $x = 0$ ,  $a = 0.05L$ ), at the otic capsule ( $x = 0.19L$ ,  $a = 0.005L$ ), at the base of the tail ( $x = 0.384L$ ,  $a = 0.04L$ ), at the mid tail ( $x = 0.692L$ ,  $a = 0.1L$ ) and at the tail tip ( $x = 1.0L$ ,  $a = 0.2L$ ). More details can be found in Liu, 1997.

The kinematic model of a moth-flapping wing was built on a basis of a Fourier series expression of the kinematics of a hovering hawkmoth, *Manduca sexta* (Liu and Kawachi, 1998). The body-fixed system ( $x$ ,  $y$ ,  $z$ ) has its origin at the wing base, with the  $x$ -axis normal to the stroke plane, the  $y$ -axis vertical to the body axis, and the  $z$ -axis parallel to the stroke plane. 3D movements of the wing consist of three basic motions (1) flapping about the  $x$ -axis in the stroke plane described by the positional angle; (2) rotation of the wing, about the  $z$ -axis, out of the stroke plane on either side described by the elevation angle; (3) rotation (feathering) of the forewing (leading edge) and hind wing (trailing-edge) with respect to the stroke plane by varying the angle of attack of the forewing and the angle of attack of the hind wing.

The time variation of these instantaneous angles during one flapping cycle is plotted in Figure 4. The parameter  $K$  is defined as the reduced frequency by  $2\pi f c_m / 2U_{ref}$ , where  $f$  is flapping frequency;  $c_m$  is the mean wing chord length used as the reference length, and  $U_{ref}$  is reference velocity at the radius of the second moment of wing area ( $r_2$ : as a fraction of wing length  $R$ ). The reference velocity equals  $\omega r_2 R$ , where  $\omega$  is the mean angular velocity of the wing ( $\omega = 2\Phi f$ , where  $\Phi$  is the wing beat amplitude). The Reynolds number is defined as,  $Re = c_m U_{ref} / \nu$ , where  $\nu$  is kinematic viscosity of air,  $1.5 \times 10^{-5} \text{ m}^2/\text{sec}$ . For the hawkmoth  $c_m = 1.83 \text{ cm}$ ,  $r_2 = 0.52$ ,  $R = 4.83 \text{ cm}$ ,  $\omega = 2.0 \text{ rad}$ ,  $f = 26.1 \text{ sec}^{-1}$ , so  $Re$  is approximately 4,000, and the reduced frequency  $K$  was 0.37.

#### Computational fluid dynamic modeling

The governing equations are the three-dimensional, incompressible, unsteady Navier-Stokes equations written in strong conservation form for mass and momentum. The artificial compressibility method is used by adding a pseudo time derivative of pressure to the equation of continuity. For an arbitrary deformable control volume  $V(t)$ , the nondimensionalized governing equations are

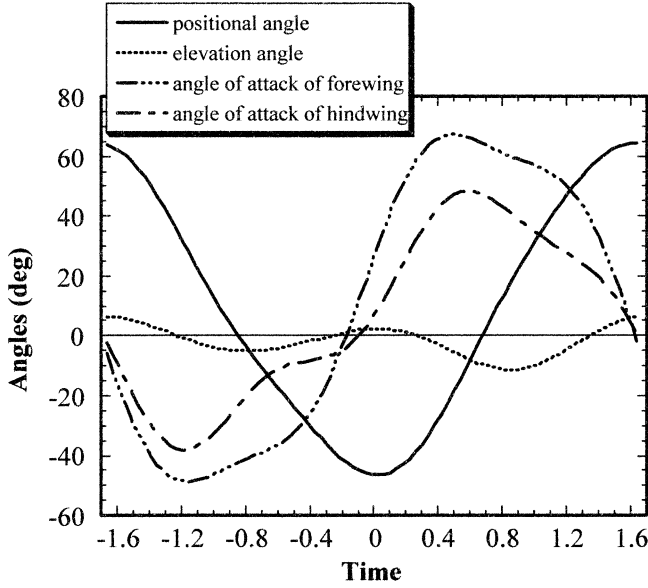


FIG. 4. Time variation of positional angle, elevation angle, angles of attack of forewing, and angles of attack of hind wing.

$$\int_{V(t)} \left( \frac{\partial \mathbf{Q}}{\partial t} + \frac{\partial \mathbf{q}}{\partial \tau} \right) dV + \int_{V(t)} \left( \frac{\partial \mathbf{F}}{\partial x} + \frac{\partial \mathbf{G}}{\partial y} + \frac{\partial \mathbf{H}}{\partial z} + \frac{\partial \mathbf{F}_v}{\partial x} + \frac{\partial \mathbf{G}_v}{\partial y} + \frac{\partial \mathbf{H}_v}{\partial z} \right) dV = 0, \quad (2)$$

where

$$\mathbf{Q} = \begin{bmatrix} u \\ v \\ w \\ 0 \end{bmatrix}, \quad \mathbf{q} = \begin{bmatrix} u \\ v \\ w \\ p \end{bmatrix}, \quad \mathbf{F} = \begin{bmatrix} u^2 + p \\ uv \\ uw \\ \beta u \end{bmatrix}$$

$$\mathbf{G} = \begin{bmatrix} vu \\ v^2 + p \\ vw \\ \beta v \end{bmatrix}, \quad \mathbf{H} = \begin{bmatrix} wu \\ wv \\ w^2 + p \\ \beta w \end{bmatrix}$$

$$\mathbf{F}_v = -\frac{1}{Re} \begin{bmatrix} 2u_x \\ u_y + v_x \\ u_z + w_x \\ 0 \end{bmatrix}, \quad \mathbf{G}_v = -\frac{1}{Re} \begin{bmatrix} v_x + u_y \\ 2v_y \\ v_x + w_y \\ 0 \end{bmatrix}$$

$$\mathbf{H}_v = -\frac{1}{Re} \begin{bmatrix} w_x + u_z \\ w_y + v_z \\ 2w_z \\ 0 \end{bmatrix}.$$

In the preceding equations,  $\beta$  is the pseudo-compressibility coefficient;  $p$  is pressure;  $u$ ,  $v$ , and  $w$  are velocity components in Cartesian coordinate system  $x$ ,  $y$ , and  $z$ ;  $t$  denotes physical time and  $\tau$  is pseudo time.  $Re$  is the Reynolds number, and  $\nu_t$  is the eddy viscosity in turbulence simulation. Note that the term  $\mathbf{q}$  associ-

ated with the pseudo time is designed for an inner-iteration at each physical time step, and will vanish when the divergence of velocity is driven to zero so as to satisfy the equation of continuity.

Time-dependent solutions to the incompressible Navier-Stokes equations are formulated in the ALE (Arbitrary Lagrangian-Eulerian) manner using the finite volume method and are performed in a time-marching manner using the pseudo-compressibility method, with special treatment in the conservation of mass and momentum both in space and in time. A third-order upwind differencing scheme, using the flux-splitting method, is implemented for the convection terms in a MUSCL fashion. The viscous terms are evaluated using a second-order central differencing method based on Gaussian integration in a manner of the finite volume method. An implicit approximation-factorization method, based on the Euler implicit scheme, is employed for the time integration. More details can be found in Appendix I.

The computational domain about a swimming fish or flying insect generally consists of a moving and/or deforming body surface, an upstream and a downstream. At the upstream velocity components are fixed to be uniform in steadily locomotion or zero in hovering, and  $v = w = 0$  while pressure is set to zero. At the downstream zero-gradient condition is taken for both velocity and pressure, *i.e.*,  $\partial(u, v, w, p)/\partial \mathbf{n} = 0$ . On the body surface, the no-slip condition is used for the velocity components. To incorporate the dynamic effect due to the acceleration of the oscillating body (moving and/or deforming body surface), pressure divergence at the surface stencils is derived from the local momentum equation, such that

$$(u, v, w) = (u_{body}, v_{body}, w_{body})$$

$$\partial p / \partial n = -\mathbf{a}_o \cdot \mathbf{n}, \quad (3)$$

where the velocity  $(u_{body}, v_{body}, w_{body})$  and the acceleration  $(\mathbf{a}_o)$  on the solid wall are evaluated and updated using the renewed grids on the fin surface at each time step.

#### Verification and validation

A variety of validation tests were undertaken to assess the reliability of the present methodology and code, which can be found in (Liu and Kawachi, 1998; Liu, 1999). Physics of fluids around locomotive animals of both fish swimming and insect and bird flapping flight is often of a dynamic vortex structure as their bodies, fins and wings usually perform periodically oscillating motions. Also, as we do not have experimental data of complicated flow around a realistic model, extensive study of flows around an oscillating foil can be an adequate conceptual model for the verification, validation and uncertainties of the modeling of actual reality, the algorithm and the code in resolving the essential feature of such dynamic vortex flows. The mechanism of oscillating body corresponding to a thrust-generating body was numerically analyzed by

a series of stepwise computations of flows around an airfoil pitching in a uniform flow at a variety of Reynolds numbers (Liu and Kawachi, 1998, 1999).

## RESULTS AND DISCUSSIONS

### *CFD modeling of insect flapping flight*

Based on a series of numerical studies (Liu and Kawachi, 1998; Liu *et al.*, 1998) of the unsteady aerodynamics of insect flapping-wing flight, we highlight the characteristics of the dynamic vortex flow around a flapping insect wing of hovering hawkmoth via Figure 5a–d, which shows the vortex structures during a complete flapping cycle where vortices were visualized by instantaneous streamlines released from the upper wing surface and negative pressure contours in which red denotes high while blue represents low pressure. The simulated flow field around the flapping wing at downstroke was in excellent agreement with the smoke-visualized results around an artificial flapper (Ellington, 1998). A coherent leading-edge vortex with axial flow was detected during translational motions of both the up- and downstrokes. The attached leading-edge vortex causes a negative pressure region, and hence is responsible for enhancing the lift production. The axial flow, which is derived from the spanwise pressure gradient, stabilizes the vortex and gives it a characteristic spiral conical shape. The leading-edge vortex created during previous translational motion remained attached during the rotational motions of pronation and supination. Estimation of the forces during one complete flapping cycle shows that lift is produced mainly during the downstroke and the latter half of the upstroke, with little force generated during pronation and supination. The stroke plane angle that satisfies the horizontal force balance of hovering is  $23.6^\circ$ , which shows an excellent agreement with observed angles of  $20.0^\circ \sim 25.0^\circ$ .

During most of the downstroke (Fig. 5a), an intense, conical spiral leading-edge vortex is detected with strong axial flow at the core. This leads to a steadily increasing negative pressure region on the upper wing surface and hence augmentations of the lift force. During the latter half of the downstroke, another leading-edge vortex is observed at the wing tip (Fig. 5b), which also shows a spiral flow at the core but is running towards the base. Although combination of these two vortices results in very large lift force this second vortex could not be detected in the airflow visualization since they only released smoke from the leading edge over the inner half of the forewing. During the subsequent supination, the two vortices change their shapes gradually, and as the wing approaches the bottom of the wing stroke, combined with a tip vortex appearing during early supination, form a hook-shaped vortex (Fig. 5b). During the latter half of supination, the vortices are strongly deformed, quickly collapse beyond the mid-span joint of the two leading-edge vortices, and virtually shed out from the trailing edge. This was also observed in the flow visualization ex-

periments of a tethered peacock butterfly. During the early upstroke, there is no leading-edge vortex observed, and the flow is quite smooth flowing over both the upper and lower surfaces. When the wing proceeds to the latter half of the upstroke, a leading-edge vortex (Fig. 5c) appears with a comparable size to those observed during the first half of the downstroke. During the pronation, the upstroke leading-edge vortex (Fig. 5d) is still observed rolling over the leading-edge but is not located on the upper surface as could be expected if it were produced by the rotational circulation mechanism during the pronation. A trailing-edge vortex is also observed below the lower surface due to the wing rotation during the first half of the pronation. Additionally, a shear layer vortex is observed on the upper surface, stretching from the base to the tip. When the wing is ready to start the translational motion of downstroke, all the vortices observed during the pronation are shed and thus the wing, in order to have some mechanism to enhance the life-generation during the downstroke, must produce a new leading-edge vortex. Estimation of the forces during one complete flapping cycle shows that approximately 80% lift force (Liu and Kawachi, 1998; Liu *et al.*, 1998) is produced during the downstroke and the latter half of the upstroke, and hence that the leading-edge vortex particularly at the downstroke is responsible for generating the lift force for insect to stay airborne. A mean lift force during one complete flapping cycle is calculated to be comparable to the weight (1.5 g) of the hawkmoth.

This modeling of the unsteady aerodynamics of a real flapping wing has established the importance of accurately predicting the existence and timing of occurrence of the complex vortex structure and the leading-edge vortex in particular. The present results also point to the importance of the existence of a very sophisticated lift-enhancement mechanism due to the spiral leading-edge vortex at low Reynolds numbers appropriate to insect flight.

### *Implications for Micro Air Vehicle*

There is a growing recognized need for miniature flight vehicles with multifunctional capabilities, such as Micro Air Vehicles (MAVs) with wing spans of 15 cm or less, and flight speed of 30 to 60 kph which are of interest for military and civilian applications (Shyy, 2000). Our knowledge of how to design conventional fixed-wing aircraft with moderate-aspect-ratio is very likely not directly applicable to in designing such MAVs or smaller flight vehicles because the aerodynamic performance of stationary airfoils at such low Reynolds numbers (ranging over  $10^3$ – $10^5$ ) becomes worse. Flapping-wing flight of insects provides us with a sophisticated example of utilizing unsteady aerodynamics to mechanize the miniature flight structures. However, aerodynamic performance of airfoils and wings at low Reynolds numbers ( $<10^4$ ) greatly depends upon the features of the leading edge bubbles, *i.e.*, the Leading-edge vortices (LEV), which can be largely affected by both three-dimensional geometry



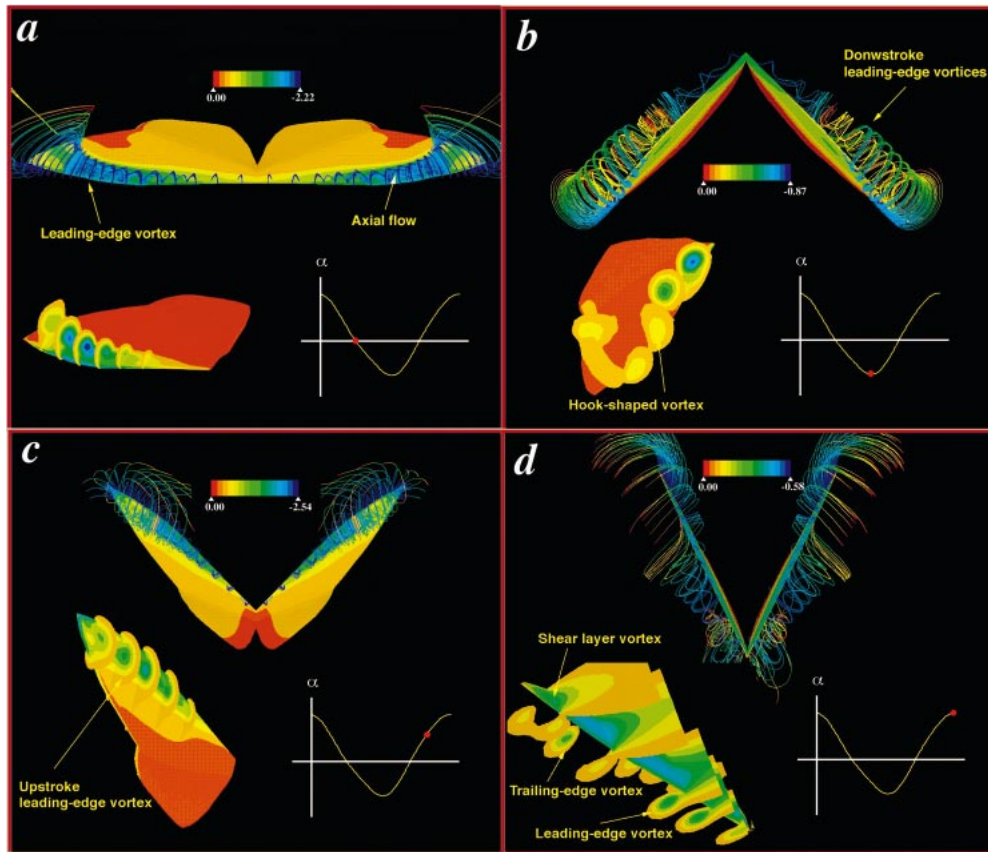


FIG. 5. Vortex structure in hawkmoth flight: a) at downstroke; b) at supination; c) at upstroke; and d) at pronation.

and the wing dynamics. LEVs can also be found in the case of fixed airfoils and wings (Gursul and Ho, 1992; Sunada *et al.*, 1997; Ikehata *et al.*, 1997; Wu *et al.*, 1991) but are quite unstable in general, resulting in large-scale separation and reattachment that is difficult to control merely through optimal selection of the profile. However, as often seen in insect and bird flight, appropriate active control of the wing motion, or kinematics, can be an efficient way of achieving high and stable lift generation. One of the successful man-made aircraft that actively utilizes the wing motion is the rotary blade helicopter. However, whether the rotary wing (blade) still works well at the size of insect and bird wings, or, if not, how its aerodynamic characteristics change, is not clear yet.

For the rotary wing, the same geometric model is utilized but in a steadily rotating mode with respect to the axis  $z$ . The Reynolds number and the reduced frequency are identical to the flapping wing model. In the rotating frame of reference, flows around the rotary wing may be solved by computing the flows around a wing, which starts impulsively from rest, advancing forward with a spanwise gradient of oncoming velocity. The rotary wing model rotates with respect to the axis  $z$ , at angles of attack ranging over  $10^\circ$ – $60^\circ$ . The angular velocity of rotation is taken equal to the maximum achieved by the flapping hawkmoth wing. Figure 6 shows the visualized LEVs structure. Unlike the

typical stall of stationary airfoils at high Reynolds number ( $>10^6$ ), the lift coefficient does not drop even at very large angles of attack ( $>40^\circ$ ). Figure 6a–f clearly identify the leading edge vortex as the source of lift generation at this moderate Reynolds number: the vortex is constantly created, and it grows with increasing angle of attack but does not collapse; correspondingly, a negative pressure region is induced on the leading edge, which is responsible for the lift generation.

The vortices when they initiate at the leading edge are quite 2D in structures but have larger sizes in moving toward the wing tip, which is thought to be due to the rotation-based potential velocity gradient in the spanwise direction. The LEV is subject to a combination of the centrifugal force, the Coriolis force, the dynamic pressure gradient corresponding to the spanwise velocity gradient, and the pressure gradient through the cores of the LEVs, which originates from the LEV itself. Eventually, the LEVs become a characteristic spiral 3D shape with apparent axial (radial) flow at their cores (Fig. 6) as observed in the flapping wing (Fig. 5). The LEVs tend to enlarge in size with increasing angle of attack, and apparently initiate shedding at the wing tip toward the wing base, for larger angles of attack exceeding  $30^\circ$ . This indicates that the axial flow at the core of LEV may play a key role in stabilizing the vortices and hence delaying the stall.

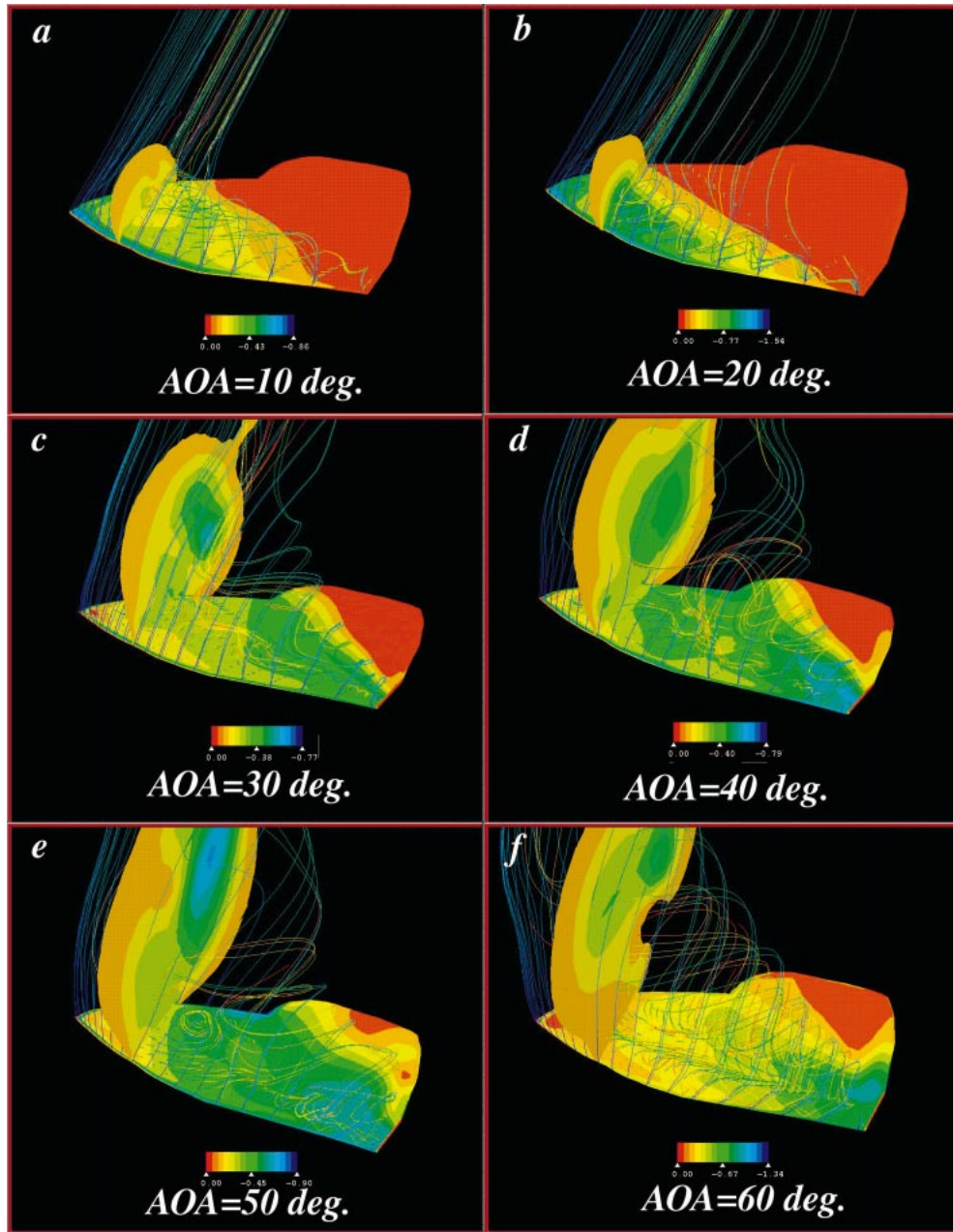


FIG. 6. Flow visualization of LEVs around a rotary moth wing. *a*, at angle of attack of 10°; *b*, at angle of attack of 20°; *c*, at angle of attack of 30°; *d*, at angle of attack of 40°; *e*, at angle of attack of 50°; and *f*, at angle of attack of 60°.

This result also supports the observation of a stall delay phenomenon associated with a propeller from Himmelskamp's experimental work by way of Schlichting (Schlichtings, 1979; Harris, 1966; Corrigan and Schlichting, 1994), which indicated that in moving toward the center of the rotor, *i.e.*, the wing base, the stall delay became more and more pronounced.

The leading-edge vortices induced by flapping and rotary wings at low Reynolds number can then be clarified as follows: 1) rotary wings as well as flapping wings can generate a conical spiral LEV with axial flow that is dominated by the *potential* spanwise ve-

locity gradient due to rotation; 2) the axial flow at the core of the LEV can delay stall and hence leads to stable lift generation with large 'apparent' stalling angle of approximately 30° and 3) a spanwise pressure gradient originating from the LEV itself creates the axial flow at the core of the LEV of both flapping and rotary wings.

#### CONCLUSION

This review gives a detailed description of the methodology of the simulation-based biological fluid dynamics and its applications in animal locomotion. Biological system in swimming and flying is, in general,



of “Complex Systems,” although some mechanisms behind it may be quite simple if unveiled, but it needs to be modeled as realistic as possible so that we could avoid some pitfalls. Compared with conventional theories and experimental methods, the simulation-based biological fluid dynamics show great potential to elucidate the physics and mechanisms in the complicated biological fluid phenomena. This new paradigm provides us not only an efficient method in deepening our understanding of biological mechanisms but also a useful tool for designing man-made vehicles as UAV/UMV (Unmanned Air or Marine Vehicle) and MAV (Micro Air Vehicle).

#### ACKNOWLEDGMENTS

The author gives special thanks to Dr. K. Kawachi, Dr. C. P. Ellington, Dr. R. Wassersug, Dr. S. Sunada, and Dr. W. Shyy for their invaluable suggestions and comments on the present works. This work was partially supported by the Japan Science and Technology Corporation (JST).

#### REFERENCES

- Azuma, A. 1983. Local momentum and local circulation methods for fixed, rotary and beating wings. Inst. Of Interdisciplinary Research, Faculty of Engineering, Univ. of Tokyo.
- Cheng, J. Y., L. X. Zhuang, and B. G. Tong. 1991. Analysis of swimming three-dimensional waving plates. *J. Fluid Mech.* 232: 341–355.
- Cloupeau, M. 1979. Direct measurements of instantaneous lift in desert locust; comparison with Jensen's experiments on detached wings. *J. Exp. Biol.* 180:1.
- Corrigan, J. J. and H. Schlichting. 1994. Empirical Model for Stall Delay due to Rotation, Proceedings of the American Helicopter Society Aeromechanics Specialists Conference, San Francisco, California Jan. 19–21.
- Dickinson, M. H., F. O. Lehmann, and S. P. Sane. 1999. *Science* 284:1954–1960.
- Domenici, P. and R. Blake. 1997. The kinematics and performance of fish fast-start swimming. *J. Exp. Biol.* 200:1165–1178.
- Druker, E. G. and J. V. J. Lauder. 1999. Locomotor forces on a swimming fish: Three-dimensional vortex wake dynamics quantified using digital particle image velocimetry. *J. Exp. Biol.* 202: 2393–2412.
- Druker, E. G. and J. V. J. Lauder. 2001. Wake dynamics and fluid forces of turning maneuvers in sunfish fish. *J. Exp. Biol.* 202: 2393–2412.
- Ellington, C. P. 1995. Unsteady aerodynamics of insect flight. In C. P. Ellington and T. J. Pedley (eds.), *Biological fluid dynamics*. Symp. Soc. Exp. Biol. 49:109.
- Ellington, C. P., C. Van Den Berg, A. P. Willmott, and A. L. R. Thomas. 1998. Leading-edge vortices in insect flight. *Nature* 384:626.
- Gursul, I. and C. M. Ho. 1992. High aerodynamic loads on an airfoil submerged in an unsteady stream. *AIAA J.* 30(4):1117–1120.
- Harris, F. D. 1996. Preliminary study of radial flow effects on rotor blades. *J. Am. Helicopter Soc.* 11(3).
- Ikehata, M., T. Inoue, M. Ozawa, and S. Matsumoto. 1997. Experimental investigation on flow fields of viscous fluid around two-dimensional wings comparison with computational results,” *J. Mar. Sci. Technol.* 2:62–76.
- Johnson, T. P., A. J. Cullum, and A. F. Bennett. 1998. Partitioning the effects of temperature and kinematic viscosity on the C-start performance of adult fishes. *J. Exp. Biol.* 201:2045–2051.
- Lighthill, M. J. 1969. Hydrodynamics of aquatic animal locomotion. *Ann. Rev. Fluid Mech.* 1:413–446.
- Lighthill, M. J. 1975. *Mathematical biofluidynamics*. SIAM, Philadelphia.
- Liu, H. 1995. A numerical study of jet-stream propulsion of oscillating bodies. *J. Soc. Naval Architects. Jpn.* 178:101–112.
- Liu, H., C. P. Ellington, K. Kawachi, C. Van Den Berg, and A. P. Willmott. 1998. A computational fluid dynamic study of hawk-moth hovering. *J. Exp. Biol.* 201:461–477.
- Liu, H. and K. Kawachi. 1998. A numerical study of insect flight. *J. Comput. Phys.* 146(1):124–156.
- Liu, H. and K. Kawachi. 1999. A numerical study of undulatory swimming. *J. Comput. Phys.* 155:223–247.
- Liu, H. and K. Kawachi. 2001. Leading-edge vortices of flapping and rotary wings at low Reynolds Number, AIAA Book, Special issue on *Fixed, Flapping and Rotary Wings at Low Reynolds Numbers*. AIAA. Progress in Astronautics and Aeronautics. 195:275–285.
- Liu, H., S. Sunada, and K. Kawachi. 1995. Unsteady solutions to the incompressible Navier Stokes equations with the pseudo-compressibility method. *ASME-FED* 215:105–112.
- Liu, H., R. Wassersug, and K. Kawachi. 1996. A computational fluid dynamic study of tadpole swimming. *J. Exp. Biol.* 199(6): 1024–1260.
- Liu, H., R. Wassersug, and K. Kawachi. 1997. Three-dimensional hydrodynamics of tadpole swimming. *J. Exp. Biol.* 200(4): 2356–2368.
- Maxworthy, T. 1979. Experiments on the Weis-Fogh mechanism of lift generation by insects in hovering flight. Part 1. Dynamics of the ‘fling’. *J. Fluid Mech.* 93:47.
- Newman, J. N. 1973. The force on a slender fish-like body. *J. Fluid Mech.* 58(4):689–702.
- Norberg, U. M. 1990. *Vertebrate flight*. Springer-Verlag, Berlin.
- Pennycuik, C. J. 1989. *Bird flight performance, a practical calculation manual*. Oxford University Press, Oxford.
- Rayner, J. M. V. 1979. A vortex theory of animal flight. *J. Fluid Mech.* 91:697.
- Schlichting, H. 1979. *Boundary layer theory*, 7th ed. McGrawHill, New York.
- Shyy, W., M. Berg, and D. Ljungqvist. 1999. Flapping and flexible wings for biological and micro air vehicles, *Progress in Aerospace Sciences*, 35(5):455–506.
- Spedding, G. R. 1992. *The aerodynamics of flight*. In R. McN. Alexander (ed.), *Adv. Comp. Physiol. The Mechanics of Animal Locomotion*. Springer-Verlag, 51.
- Sunada, S., A. Sakaguchi, and K. Kawachi. 1997. Airfoil section characteristics at a low Reynolds Number. *J. Fluid Eng.* 119: 129–135.
- Triantafyllou, M. S. and G. S. Triantafyllou. 1995. An efficient swimming machine. *Sci. Amer.* 3:1–26.
- Triantafyllou, G. S., M. S. Triantafyllou, and M. A. Grosenbaugh. 1993. Optimal thrust development in oscillating foils with application to fish propulsion. *J. Fluid & Struc.* 7:205–224.
- Weis-Fogh, T. 1972. Energetic of hovering flight in hummingbirds and in *Drosophila*. *J. Exp. Biol.* 56:79.
- Wilkin, P. J. and H. M. Williams. 1993. Comparison of the aerodynamic forces on a flying sphingid moth with those predicted by quasi-steady theory. *Physiol. Zool.* 66:1015.
- Wu, T. Y. 1971. Hydrodynamics of swimming propulsion. Part 3. Swimming and optimum movements of slender fish with side fins. *J. Fluid Mech.* 46(3):545–568.
- Wu, J. E., A. D. Vakili, and J. M. Wu. 1991. Review of the physics of enhancing vortex lift by unsteady excitation. *Prog. Aerospace Sci.* 28:73–131.

#### APPENDIX I

By introducing the generalized Reynolds transport theorem and by employing the Gauss integration theorem to the first and second integrals in Eq. (2), respectively, an integrated form of the governing equations in general curvilinear co-ordinate system is gained as

$$\int_{V(t)} \frac{\partial \mathbf{q}}{\partial \tau} dV + \frac{\partial}{\partial t} \int_{V(t)} \mathbf{Q} dV + \oint_{S(t)} (\mathbf{f} - \mathbf{Q} \mathbf{u}_s) \cdot \mathbf{n} dS = 0, \quad (\text{A1})$$

where  $\mathbf{f} = (\mathbf{F} + \mathbf{F}_v, \mathbf{G} + \mathbf{G}_v, \mathbf{H} + \mathbf{H}_v)$ ;  $S(t)$  denotes the surface of the control volume;  $\mathbf{n} = (\mathbf{n}_x, \mathbf{n}_y, \mathbf{n}_z)$  are components of the unit outward normal vector corresponding to all the faces of the polyhedron cell;  $\mathbf{u}_g$  is the local velocity of the moving cell surface. The relationship between the physical and computational spaces is given as:

$$\begin{cases} \xi = \xi(x, y, z, t) \\ \eta = \eta(x, y, z, t) \\ \zeta = \zeta(x, y, z, t) \\ t^* = t \end{cases} \Leftrightarrow \begin{cases} x = x(\xi, \eta, \zeta, t^*) \\ y = y(\xi, \eta, \zeta, t^*) \\ z = z(\xi, \eta, \zeta, t^*) \\ t = t^* \end{cases} \quad (\text{A2})$$

where  $t^*$  denotes the time in computational space  $(\xi, \eta, \zeta)$ . The last term in Eq. (A1) expresses the net flux across the cell faces. For a structured, boundary-fitted, and cell-centered storage architecture, we can further reform Eq. (A1) in terms of the semi-discrete form, where  $(i, j, k)$  denote the cell index, such that

$$\frac{\partial}{\partial t} [V_{ijk} \mathbf{Q}_{ijk} + \mathbf{R}_{ijk} + V_{ijk} \left( \frac{\partial \mathbf{q}}{\partial t} \right)_{ijk}] = 0, \quad (\text{A3})$$

where

$$\begin{aligned} \mathbf{R}_{ijk} &= (\hat{\mathbf{F}} + \hat{\mathbf{F}}_v)_{i+(1/2),j,k} - (\hat{\mathbf{F}} + \hat{\mathbf{F}}_v)_{i-(1/2),j,k} \\ &\quad + (\hat{\mathbf{G}} + \hat{\mathbf{G}}_v)_{i,j+(1/2),k} - (\hat{\mathbf{G}} + \hat{\mathbf{G}}_v)_{i,j-(1/2),k}, \quad e.g. \\ \hat{\mathbf{F}} + \hat{\mathbf{F}}_v &= (\mathbf{f} - \mathbf{Q} \mathbf{u}_g) \cdot \mathbf{S}_n^\xi \\ &\quad + (\hat{\mathbf{H}} + \hat{\mathbf{H}}_v)_{i,j,k+(1/2)} - (\hat{\mathbf{H}} + \hat{\mathbf{H}}_v)_{i,j,k-(1/2)} \\ \mathbf{S}_n^\xi &= [\mathbf{S}_{nx}^\xi, \mathbf{S}_{ny}^\xi, \mathbf{S}_{nz}^\xi] \mathbf{n} = [\mathbf{S}_{nx}^\xi, \mathbf{S}_{ny}^\xi, \mathbf{S}_{nz}^\xi] / S, \\ S &= \sqrt{S_{nx}^2 + S_{ny}^2 + S_{nz}^2}. \end{aligned}$$

The term  $V_{ijk}$  is the volume of the cell  $(i, j, k)$ . Note that the unit outward normal vector  $\mathbf{n}$  can be calculated using the areas of the cell faces, e.g.,  $\mathbf{S}_n^\xi$  in  $\xi$ -direction. A detailed description of evaluation of the inviscid flux and the viscous flux can be found in Liu and Kawachi (1998).

The Pade scheme is employed for the time integration

$$\frac{\partial}{\partial t} = \frac{1}{\Delta t} \frac{\Delta}{1 + \theta \Delta}, \quad \text{or} \quad \frac{\Delta(V\mathbf{Q})_{ijk}^{(n+1)} - \Delta(V\mathbf{Q})_{ijk}^{(n)}}{\Delta t} = - \left\{ \mathbf{R}_{ijk} + V_{ijk} \left( \frac{\partial \mathbf{q}}{\partial t} \right)_{ijk} \right\}^{(n+1)} \quad (\text{A4})$$

where parameter  $\theta$  is taken to be 1 for the implicit Euler scheme with first-order accuracy in time;  $\Delta t$  is the time increment; and  $\Delta \mathbf{q} = \mathbf{q}^{(n+1)} - \mathbf{q}^{(n)}$ . Thus, Eq. (A3) can be discretized by replacing the time-related term with Eq. (A4), such that

$$\begin{aligned} \Delta(V\mathbf{Q})_{ijk}^{(n)} + \theta \Delta t \Delta \left[ \mathbf{R}_{ijk} + V_{ijk} \left( \frac{\partial \mathbf{q}}{\partial t} \right)_{ijk} \right]^{(n)} \\ = - \Delta t \left[ \mathbf{R}_{ijk} + V_{ijk} \left( \frac{\partial \mathbf{q}}{\partial t} \right)_{ijk} \right]^{(n)}. \end{aligned} \quad (\text{A5})$$

Since the volume of the cell may change with time due to the moving grid system, we assess the first term in the Eq. (A5) as

$$\begin{aligned} \Delta(V\mathbf{Q})_{ijk}^{(n)} &= (V\mathbf{Q})_{ijk}^{(n+1)} - (V\mathbf{Q})_{ijk}^{(n)} \\ &= V_{ijk}^{(n+1)} \Delta \mathbf{Q}_{ijk}^{(n)} + \Delta V_{ijk}^{(n)} \mathbf{Q}_{ijk}^{(n)} \\ &\approx V_{ijk}^{(n)} \Delta \mathbf{Q}_{ijk}^{(n)} + \Delta V_{ijk}^{(n)} \mathbf{Q}_{ijk}^{(n)}. \end{aligned} \quad (\text{A6})$$

A problem rises here as to how to satisfy the so-called ‘‘Geometric Conservation Law (GCL)’’, i.e., the conservation of momentum taken into the Newton laws at each time step in term of evaluation of the increment of the volume  $\Delta V_{ijk}(n)$  for the moving grid system.

Considering the conservation of flux across the cell faces in an extreme case of solving uniform flow with the moving grid system,  $\Delta V_{ijk}(n)$  can be explicitly expressed by substituting Eq. (A6) into Eq. (A5), such that,

$$\begin{aligned} \Delta V_{ijk}^{(n)} &= \Delta t [(u_g \cdot \mathbf{S}_n^\xi)_{i+(1/2)} - (u_g \cdot \mathbf{S}_n^\xi)_{i-(1/2)} + (u_g \cdot \mathbf{S}_n^\eta)_{j+(1/2)} \\ &\quad - (u_g \cdot \mathbf{S}_n^\eta)_{j-(1/2)} + (u_g \cdot \mathbf{S}_n^\zeta)_{k+(1/2)} \\ &\quad - (u_g \cdot \mathbf{S}_n^\zeta)_{k-(1/2)}] \end{aligned} \quad (\text{A7})$$

The pseudo time-related terms designed for the inner-iteration can be approximated as

$$\begin{aligned} \theta \Delta t \Delta \left( V_{ijk} \frac{\partial \mathbf{q}}{\partial \tau} \right)^{(n)} + \Delta t \left( V_{ijk} \frac{\partial \mathbf{q}}{\partial \tau} \right)^{(n)} \\ = \Delta t \left[ (1 - \theta) \left( V_{ijk} \frac{\partial \mathbf{q}}{\partial \tau} \right)^{(n)} + \theta V_{ijk}^{(n+1)} \frac{\partial \mathbf{q}^{(n+1)}}{\partial \tau} \right] \\ \approx \Delta t V_{ijk}^{(n)} \frac{\partial \mathbf{q}^{(n)}}{\partial \tau} \end{aligned} \quad (\text{A8})$$

Note that, in the preceding Eq. (A8), the approximation  $(\partial \mathbf{q}^{(n)} / \partial \tau) = \partial \mathbf{q}^{(n+1)} / \partial \tau$  is reasonable because the pseudo time  $\tau$  is for the inner-iteration and thus is dependent at each physical time step. Hence, the governing equations become

$$\frac{\Delta \mathbf{Q}_{ijk}^{(n)}}{\Delta t} + \frac{\theta \Delta \mathbf{R}_{ijk}^{(n)}}{V_{ijk}^{(n)}} + \frac{\partial \mathbf{q}^{(n)}}{\partial \tau} = - \frac{\mathbf{R}_{ijk}^{(n)}}{V_{ijk}^{(n)}} - \frac{\Delta V_{ijk}^{(n)}}{\Delta t V_{ijk}^{(n)}} \mathbf{Q}_{ijk}^{(n)} \quad (\text{A9})$$

The implicit Euler scheme is also employed for the pseudo time integration. With the differencing operator for the pseudo time, the governing equations can be reformd as

$$\begin{aligned} \left\{ \frac{\mathbf{I}}{\Delta \tau} + \theta \frac{\mathbf{I}_a}{\Delta t} \left( 1 + \frac{\Delta V_{ijk}^{(n)}}{V_{ijk}^{(n)}} \right) + \frac{\theta}{V_{ijk}^{(n)}} \frac{\partial \mathbf{R}_{ijk}^{(n,m)}}{\partial \mathbf{q}} \right\} \Delta \mathbf{q}_{ijk}^{(n,m)} \\ = - \frac{1}{V_{ijk}^{(n)}} [(1 - \theta) \mathbf{R}_{ijk}^{(n)} + \theta \mathbf{R}_{ijk}^{(n,m)}] \\ + \frac{\mathbf{I}_a}{\Delta t} \left\{ (\mathbf{q}_{ijk}^{(n,0)} - \mathbf{q}_{ijk}^{(n,m)}) - \frac{\Delta V_{ijk}^{(n)}}{V_{ijk}^{(n)}} \mathbf{q}_{ijk}^{(n,m)} \right\}, \end{aligned} \quad (\text{A10})$$

where  $\Delta \tau$  is the pseudotime-step size and  $\mathbf{I}_a = [1, 1, 1, 0]^T$ . In order to benefit from both lower memory and computational requirements for the solution of Eq. (A10), the approximated factorization method (Liu, 1998), is used for the LHS, and hence, Eq. (A10) is rewritten as:

$$\begin{aligned} \left\{ \mathbf{I} + \frac{\theta \Delta t \mathbf{I}_a}{V_{ijk}^{(n)}} \frac{\partial \mathbf{R}_{ijk}^{(n,m)}}{\partial \mathbf{q}} \right\}^{(\xi)} \left\{ \mathbf{I} + \frac{\theta \Delta t \mathbf{I}_a}{V_{ijk}^{(n)}} \frac{\partial \mathbf{R}_{ijk}^{(n,m)}}{\partial \mathbf{q}} \right\}^{(\eta)} \\ \times \left\{ \mathbf{I} + \frac{\theta \Delta t \mathbf{I}_a}{V_{ijk}^{(n)}} \frac{\partial \mathbf{R}_{ijk}^{(n,m)}}{\partial \mathbf{q}} \right\}^{(\zeta)} \Delta \mathbf{q}_{ijk}^{(n,m)} \\ = - \frac{\Delta t \mathbf{I}_a}{V_{ijk}^{(n)}} [(1 - \theta) \mathbf{R}_{ijk}^{(n)} + \theta \mathbf{R}_{ijk}^{(n,m)}] \\ + \mathbf{I}_t \mathbf{I}_a \left\{ (\mathbf{q}_{ijk}^{(n,0)} - \mathbf{q}_{ijk}^{(n,m)}) - \frac{\Delta V_{ijk}^{(n)}}{V_{ijk}^{(n)}} \mathbf{q}_{ijk}^{(n,m)} \right\}, \end{aligned} \quad (\text{A11})$$

where  $\mathbf{I}_t = (1/(\theta + \Delta t/\Delta \tau), 1/(\theta + \Delta t/\Delta \tau), 1/(\theta + \Delta t/\Delta \tau), \Delta \tau/\Delta t)$ , a diagonal matrix. The term associated with the change of volume of the LHS is neglected, which does not affect the accuracy of solution when it converges. Note that taking a infinity pseudo time step  $\Delta \tau$  reduces the  $\mathbf{I}_t$  to a unit matrix, which can accelerate the convergence of the inner-iteration. The preceding equations can be further decomposed into three sweeps in the  $\xi$ -,  $\eta$ -, and  $\zeta$ -directions in computational domain. A linear system of equations is finally yielded, in which the discrete form of the matrix from the LHS is tridiagonally banded. (More details can found in Liu and Kawachi, 1998)